Letter

$\mathbb{Z}_2$ nontrivial topology of rare-earth binary oxide superconductor LaO

Jiahui Qian,[1] Zongqi Shen [ORCID],[1] Xinyuan Wei,[1] and Wei Li [ORCID][1,2,*]

[1]*State Key Laboratory of Surface Physics and Department of Physics, Fudan University, Shanghai 200433, China*
[2]*Collaborative Innovation Center of Advanced Microstructures, Nanjing University, Jiangsu 210093, China*

Recently, superconductivity has been discovered in rocksalt-structured binary lanthanum monoxide LaO through state-of-the-art oxide thin-film epitaxy. In this work, we reveal that the normal state of superconducting LaO is a $\mathbb{Z}_2$ nontrivial topological metal, where the Dirac point protected by the crystal symmetry is located around the Fermi energy. By analyzing the orbital characteristics, we show that the nature of the topological band structure of LaO originates from the intra-atomic transition from the outer shell La $5d$ to the inner shell $4f$ orbitals driven by the strong octahedral crystal field. Furthermore, the appearance of novel surface states unambiguously demonstrates the topological signature of the LaO superconductor. Our theoretical findings not only shed light on the understanding of the exotic quantum behaviors in the LaO superconductor with intimate correlation between $4f$ and $5d$ orbitals in La, but also provide an exciting platform to explore the interplay between nontrivial topology and superconductivity.

Introduction. The search for exotic quantum states in quantum materials is an appealing subject in condensed matter physics. Among them, rare-earth compounds show unique physical properties such as mixed-valence phenomena [1,2], Kondo insulating states [3,4], heavy-fermion behavior [5], and intriguing superconductivity [6]. In particular, the rare-earth binary compound of lanthanum superhydride LaH_{10} under extreme high pressures displays high transition temperature (T_c) superconductivity with a T_c of 260 K, which represents a step toward the goal of achieving room-temperature superconductors [7,8]. At ambient pressure, the binary lanthanum dicarbide LaC_2 shows superconductivity at 1.6 K [9]. Compared with LaC_2, the binary lanthanum sesquicarbide La_2C_3 is characterized by a higher T_c of 11 K [10,11], which can be further enhanced to 13 K by tuning the La/C ratio [12]. The inherent pairing symmetry of these binary lanthanum carbide superconductors, however, needs further scrutiny [13].

Recently, a new type of binary lanthanum monoxide LaO with rocksalt structure was reported to be a superconductor with a T_c of 5 K using state-of-the-art oxide thin-film epitaxy techniques [14], since rare-earth elements usually prefer their trivalent ionic state to form the most stable binary sesquioxides [15], which are well-known high-permittivity wide-gap insulators for gate dielectrics [16]. For metastable rare-earth monoxides, the electronic properties are significantly different from those of sesquioxides due to the presence of outer shell $5d$ conduction carriers in La atoms, which strongly interact with their localized inner shell $4f$ electrons around the Fermi energy [17]. Electronic band structure calculations have shown that the conducting electrons around the Fermi level in the LaO superconductor mainly come from the contribution of La $5d$ orbitals, strongly hybridized with the La $4f$ orbitals

[18]. This implies that the binary lanthanum monoxide superconductor LaO may lead to topologically nontrivial electronic structures driven by the La $5d$-$4f$ orbital transitions with opposite parity.

In this Letter, we revisit and discuss the nature of the interplay between La $5d$ and $4f$ orbitals in the newly discovered rare-earth binary superconductor LaO using the first-principles calculations. Our results show that the normal state of the LaO superconductor is a nontrivial $\mathbb{Z}_2$ topological metal. Interestingly, the topologically protected Dirac point is located around the Fermi energy. This originates from the inherent features of LaO, i.e., from the La $5d$-$4f$ orbital transitions driven by the strong octahedral crystal field. The existence of novel surface states further unambiguously demonstrates the topological signature of the LaO superconductor in its normal state.

Theoretical calculations. In our first-principles calculations [19–21], we employ the plane-wave basis method and the Perdew-Burke-Ernzerhof exchange correlation potential [22], as implemented in the VASP code [23]. A 600 eV cutoff in the plane-wave expansion and a $20 \times 20 \times 20$ Monkhorst-Pack **k** grid are chosen to ensure accuracy up to 10^{-5} meV. The lattice constants are optimized to make forces on individual atoms below 10^{-3} eV/Å. Furthermore, we take into account the contribution of spin-orbit coupling using the second variational method [24], and the phonon dispersion is calculated using the density functional perturbation theory within the Phonopy code [25,26].

Figure 1(a) shows the crystal structure of the LaO superconductor, which crystallizes in a face-centered-cubic (fcc) structure of rocksalt type with space group Fm-$3m$. The optimized lattice constants of LaO are 5.158 Å, in good agreement with previous experimental values (5.144 Å) [27], and with the theoretical prediction (5.164 Å) obtained using an ultrasoft pseudopotential [18]. The corresponding Brillouin zone (BZ)

*w_li@fudan.edu.cn
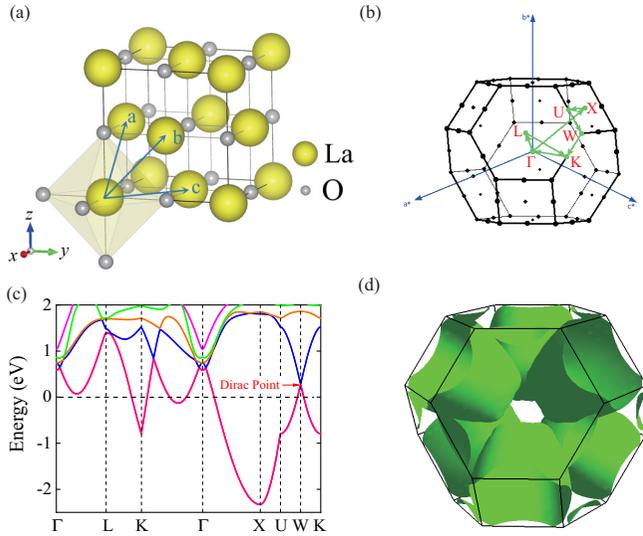
FIG. 1. (a) Crystal structure of LaO. Here **a**, **b**, and **c** are the primitive lattice vectors. (b) BZ for the primitive cell of LaO. The high-symmetry paths are indicated by the green arrows. (c) Electronic band structure of LaO along the high-symmetry paths shown in (b). The Fermi energy is set to zero in (c). (d) Corresponding Fermi surface topology.

TABLE I. Parities $\delta_{\Gamma_i}^{\kappa}$ at the κth band and the eight time-reversal invariant **k** points [one Γ $(0, 0, 0)$, three X $(\frac{1}{2}, \frac{1}{2}, 0)2\pi/a$, and four L $(\frac{1}{2}, \frac{1}{2}, \frac{1}{2})2\pi/a$] for LaO. Due to the Kramers degeneracy, we only list the parities on the even numbered bands. The nontrivial $\mathbb{Z}_2$ topological invariants are evaluated through the product of the parities $\delta_{\Gamma_i}^{\kappa}$ at the eight time-reversal invariant **k** points on a selected band with index of κ corresponding to that shown in Fig. 1(c).

	δ_Γ	$3 \times \delta_X$	$4 \times \delta_L$	$\mathbb{Z}_2$
Band 24 (green)	−1	−1	+1	(0;000)
Band 22 (orange)	+1	−1	−1	(1;000)
Band 20 (blue)	+1	−1	−1	(1;000)
Band 18 (magenta)	+1	+1	−1	(0;000)

of the primitive cell of LaO along the high-symmetry **k** point is depicted in Fig. 1(b). The stability of the optimized lattice structure of LaO is also examined by calculating the phonon spectrum, shown in Fig. S1 [28]. There are no imaginary frequencies in the phonon spectrum, confirming the dynamical stability of the rocksalt-structured lanthanum monoxide LaO.

The calculated electronic band structure of LaO is shown in Fig. 1(c) (also see Fig. S2 [28]). There is a single band passing through the Fermi level E_f across the BZ, and this suggests a metallic behavior of the LaO superconductor in the normal state [also see the Fermi surface topology in Fig. 1(d)]. This result is intuitively expected since for the La^{2+} ion in the monoxide LaO, the nominal number of the configuration La^{2+}: $5d^14f^0$ electron is 1, and thus the lowest-lying conduction band is partially occupied. In the vicinity of the Fermi level E_f, there is an intriguing Dirac point (0.2 eV above the E_f about extra 0.2 e^-) appearing at the high-symmetric W point in the BZ [31,32]. Usually, the appearance of a Dirac point in three-dimensional systems (preserving both the time-reversal and inversion symmetries), where two Weyl points overlap in momentum space, is unstable. On the other hand, the crystal symmetry of C_{4v} at the W point in the BZ protects the stability of the Dirac point in LaO (see the strained band in Fig. S3) [28,33,34]. In addition, we also notice that there is a band crossing above E_f (at 0.56 eV), indicating the existence of band inversion in the electronic band structure of LaO. Overall, these results strongly indicate that the electronic structure of the LaO superconductor in the normal state is a nontrivial topological metallic phase in three dimensions [32].

Since LaO is invariant under time-reversal symmetry (see the magnetization calculations listed in Table S1, with magnetic configurations shown in Fig. S4) [28,35–38], we have carried out the calculations of the $\mathbb{Z}_2$ topological index and quantitatively inspected the nontrivial topological phases of

LaO. Besides the spatial inversion symmetry in rocksalt-structured LaO, the calculation of the $\mathbb{Z}_2$ topological invariant can be dramatically simplified by the so-called "parity method" [39–41]. Accordingly, the $\mathbb{Z}_2$ topological invariant of LaO can be obtained from the wave-function parities $\delta_{\Gamma_i}^{\kappa}$ on a band index κ around the Fermi level E_f at the eight time-reversal invariant **k** points defined as $\Gamma_{i=(n_1n_2n_3)} = \frac{1}{2}(n_1\mathbf{a}^* + n_2\mathbf{b}^* + n_3\mathbf{c}^*)$. Here $\mathbf{a}^*$, $\mathbf{b}^*$, and $\mathbf{c}^*$ are the primitive reciprocal lattice vectors shown in Fig. 1(b) with $n_j = 0$ or 1, and determined by the quantities $\delta_{\Gamma_i}^{\kappa=2\kappa'} = \langle \Phi_{2\kappa',\Gamma_i}|\hat{P}|\Phi_{2\kappa',\Gamma_i}\rangle = \pm 1$. In turn, they are the eigenvalues of the parity operator $\hat{P}$, and correspond to even (odd) parity of the Bloch functions $|\Phi_{2\kappa',\Gamma_i}\rangle$ at the $2\kappa'$th band and time-reversal invariant **k** point Γ_i. Notice that we use the band numbering scheme from the calculations of density functional theory because LaO is a metal with no clear division between conduction and valence states, as shown in Fig. 1(c) [40–42]. For the LaO fcc lattice, we have the following eight time-reversal invariant **k** points: one Γ $(0, 0, 0)$, three X $(\frac{1}{2}, \frac{1}{2}, 0)2\pi/a$, and four L $(\frac{1}{2}, \frac{1}{2}, \frac{1}{2})2\pi/a$, shown in Fig. 1(b). The calculated parities on LaO at these time-reversal invariant **k** points with a given band index κ $(= 2\kappa')$ around the Fermi level E_f are shown in Fig. 1(c) (Kramers-degenerate bands, $\delta_{\Gamma_i}^{2\kappa'} = \delta_{\Gamma_i}^{2\kappa'-1}$) and listed in Table I. The $\mathbb{Z}_2$ topological invariants $(\nu_0; \nu_1\nu_2\nu_3)$ between each pair of bands (κ) near the Fermi level are thus evaluated as the product of these parities at the time-reversal invariant **k** points. They are defined as $(-1)^{\nu_0} = \Pi_{i=1}^{8}\delta_{\Gamma_i}^{\kappa}$ and $(-1)^{\nu_k} = \Pi_{n_k=1,n_{j\neq k}=0,1}\delta_{\Gamma_{i=(n_1n_2n_3)}}^{\kappa}$, where ν_0 is a strong topological index independent of the choice of primitive reciprocal lattice vectors Γ_j. On the contrary, ν_1, ν_2, and ν_3, referred to as weak topological indexes, do depend on the choice. Interestingly, the existence of nonzero topological indices (see Table I) allows us to identify the normal state of superconducting LaO as a $\mathbb{Z}_2$ topological metal (also see the detailed band topological invariants in Fig. S5 and Table S2) [28]. The intriguing Dirac point and band inversion shown in Fig. 1(c) occur at the transition between the trivial and nontrivial strong topological bands (see band indexes 18 and 20 listed in Table I), which confirms the inherent topological nature of the electronic state behaviors in LaO superconductor.

Having established the presence of a nontrivial topology in LaO, we now proceed to elaborate on the nature of this $\mathbb{Z}_2$ topological metallic phase. From the viewpoint of
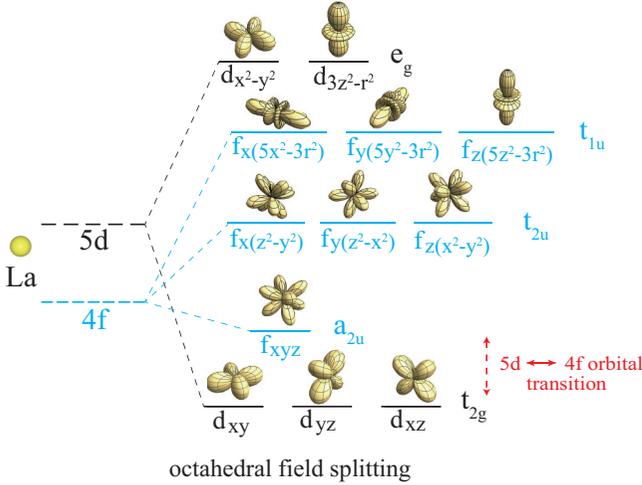
FIG. 2. Schematic diagram of the orbital evolution from the atomic outer shell $5d$ to the inner shell $4f$ orbitals of La driven by the octahedral crystal-field splitting in LaO with rocksalt structure at the Γ point in BZ. The lobes of corresponding orbitals under the symmetry of octahedral field are also sketched.

FIG. 3. (a) Total and projected DOS of La $5d$ and $4f$ and O $2p$ orbitals for LaO. (b) Projected DOS of La $5d$ and $4f$ orbitals in the presence of the octahedral field. The Fermi energy is set to zero.

ligand field theory [19,43], the lanthanum in rocksalt-structured LaO is coordinated by the oxygen octahedron [see Fig. 1(a)]. The crystal field would normally split the outer shell five degenerate $5d$ orbitals in La into the lower-lying threefold-degenerate t_{2g} composed of d_{xy}, d_{yz}, and d_{xz} orbitals, and the upper-lying twofold-degenerate e_g composed of $d_{x^2-y^2}$ and $d_{(3z^2-r^2)}$ orbitals, as schematically illustrated in Fig. 2. Furthermore, the inner shell seven degenerate $4f$ orbitals in La are also split simultaneously by the octahedral crystal field into two groups of triply degenerate orbitals [t_{1u} composed of $f_{x(5x^2-3r^2)}$, $f_{y(5y^2-3r^2)}$, and $f_{z(5z^2-3r^2)}$ orbitals, and t_{2u} composed of $f_{x(z^2-y^2)}$, $f_{y(z^2-x^2)}$, and $f_{z(x^2-y^2)}$ orbitals] and a lower-lying nondegenerate orbital (a_{2u}: f_{xyz} orbital) (also see Fig. 2). However, by considering that the charge distribution of lower-lying orbitals t_{2g} does not directly point to the oxygen anions in the octahedral crystal field, and hence their Coulomb interaction is relatively weaker than that for the a_{2u} orbital, we have that the energy of t_{2g} levels is below that of a_{2u}. As a result, the system undergoes an orbital transition between t_{2g} of $5d$ and a_{2u} of $4f$ orbitals, accompanied by parity switching (see Fig. 2). For the La^{2+} ion, the nominal number of conducting electrons is 1, which partially occupies the lowest-lying conducting band. Notice that the spin-orbit coupling has been neglected in the discussions on the orbital splitting shown in Fig. 2 because LaO is a single-band metal shown in Fig. 1(c) and the spin-orbit coupling will be significantly quenched. We have also examined the electronic band structure without inclusion of spin-orbit coupling and found that the electronic dispersion near the Fermi level remains qualitatively unaltered (see Fig. S6) [28]. This orbital splitting picture is analogous to that used in interpreting the topological Kondo insulating state in SmB$_6$ and YbB$_{12}$ [4,44,45]. Overall, we conclude that the strong octahedral crystal-field splitting drives the intra-atomic transition in energy from $5d$ to $4f$ orbitals of La, making the normal state of the LaO superconductor a nontrivial $\mathbb{Z}_2$ topological metal.
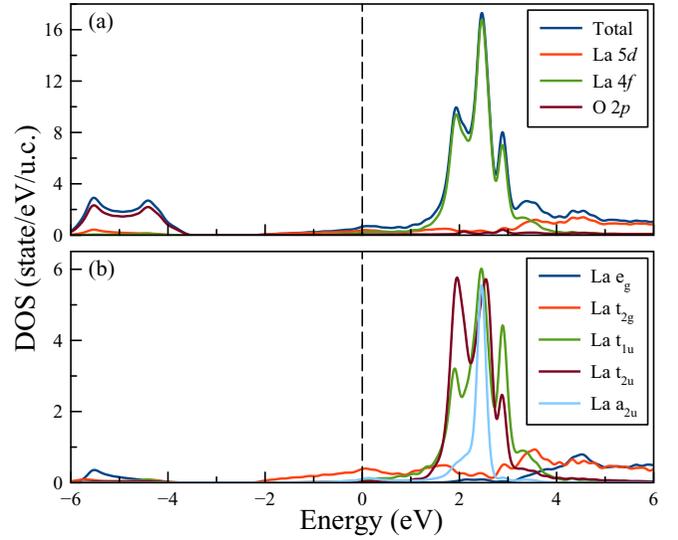
The density of states (DOS) are also evaluated to gain more insight into the aforementioned orbital splitting picture shown in Fig. 2. In Fig. 3(a), we find that the electronic states around the Fermi level E_f are mainly due to the contribution of La $5d$ orbitals hybridized strongly with La $4f$ orbitals. This result is consistent with the nature of the electron configuration of $5d^1 4f^0$ of the La^{2+} ion in the monoxide LaO, and is responsible for the intra-atomic transition from outer shell $5d$ to the inner shell $4f$ orbitals of La. Additionally, it is important to point out that there is a van Hove singularity in the vicinity of the Fermi level E_f with a DOS of 0.7 states per eV per La atom, which induces an effective reduction of the local electron Coulomb interaction, thereby enhancing the role of nonlocal electron correlations for the driving force of the appearance of superconductivity [46]. Upon inspecting the orbitally resolved DOS on La $5d$ and $4f$ orbitals, shown in Fig. 3(b), we find that the La $4f$ orbitals mainly locate inside the octahedral splitting gap $\Delta_0 \approx 2.5$ eV between the upper-lying e_g and lower-lying t_{2g} orbitals split from the La $5d$ orbitals. This is consistent with the orbital splitting picture schematically illustrated in Fig. 2 and with the fact that the octahedral crystal-field splitting gap for $5d$ orbitals is significantly larger than $4f$ ones. In the vicinity of the Fermi level E_f, we also notice that the t_{2g} orbitals play a dominant role, followed by the a_{2u} orbital. This corresponds to the trivial and nontrivial strong topological bands listed in Table I, based on the orbitally resolved electronic structure calculations, indicative of the a_{2u} orbital across the lower-lying t_{2g} orbitals resulting in the appearance of the topologically protected Dirac point (also see the orbitally resolved band in Fig. S7) [28].

Finally, we discuss the topological surface states exploiting the idea of bulk-edge correspondence of the $\mathbb{Z}_2$ topological metal [47,48]. In particular, we calculate the topological surface states of a semi-infinite system using the surface Green's function [49,50] constructed from the maximally localized Wannier function and fitting the first-principles band
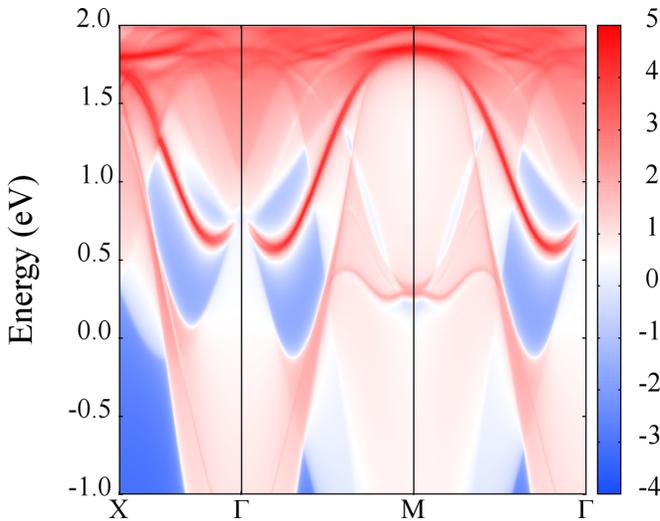
FIG. 4. The surface states of LaO projected on the (001) plane. Warmer colors denote higher local DOS and blue regions indicate the bulk band gap. The Fermi energy is set to zero.

structure calculations [51,52]. The dispersion of the surface states projected on the (001) plane, shown in Fig. 4, is obtained by evaluating the imaginary part of the surface Green's function [20,53]. Upon comparison with the bulk band structure along the [001] direction (shown in Fig. S8) [28], one clearly sees the Dirac-like topological states at the M point, slightly above the Fermi level E_f shown in Fig. 4. By unfolding the BZ, one sees that this is actually projected from the W point shown in Fig. 1(c). Additional surface states may be seen around the center of the BZ (Γ point), indicated by bright spots, which stem from the inverted band shown in Fig. 1(c) and associated with the nonzero $\mathbb{Z}_2$ numbers listed in Table I. These results on surface states further reveal the nontrivial topological electronic band structure of superconducting LaO in its normal state, and can be experimentally detected by angle-resolved photoemission spectroscopy (ARPES).

Discussion. The nontrivial $\mathbb{Z}_2$ topological band structure of three-dimensional superconducting LaO is of great interest for stabilizing the formation of Majorana modes within the vortex cores of a natively superconducting surface state that are relevant for fault-tolerant quantum computing [54–57]. Materials hosting both topologically nontrivial surface states and a native superconducting ground state are uncommon, with relatively few promising candidates identified in layered FeSe$_{1-x}$Te$_x$ [58,59] and recently discovered layered kagome superconductor CsV$_3$Sb$_5$ [40,41]. Additionally, it is worth pointing out that although the topologically protected Dirac point is located slightly above the Fermi level, the LaO system can be easily driven into such region with relatively light electron doping [about 0.2 e^- shown in Fig. 1(c)]. This may be achieved by changing the amount of oxygen vacancies in LaO thin films during deposition, which may be also used to effectively tune the critical temperature T_c [14]. On the other hand, since in three-dimensional systems the Dirac point around Fermi level E_f, see Fig. 1(c), is usually unstable, a stable and topologically protected Weyl point may originate from the Dirac point by breaking either time-reversal or inversion symmetries [31,32]. We thus suggest that Weyl superconductors may be realized using the LaO superconductor capped by a EuO ferromagnetic insulator using the proximity effect of ferromagnetism to lift the time-reversal symmetry. Alternatively, one may exploit isovalent substitution of sulfur to break the inversion symmetry [60], which can be experimentally verified by *in situ* ARPES in the near future.

Conclusion. Using the first-principles calculations on the newly discovered lanthanum monoxide superconductor (LaO), we have found that the strong electron correlation between $4f$ and $5d$ orbitals in La leads to the emergence of nontrivial topological band structure in its normal state, such as the topologically protected Dirac point around the Fermi energy and the appearance of the topological signature of novel surface states. Our theoretical study provides crucial insights into the electronic structure of superconducting LaO, thereby giving the basis for a solid understanding of the interplay between nontrivial topology and superconductivity.

[1] C. M. Varma, Mixed-valence compounds, Rev. Mod. Phys. **48**, 219 (1976).

[2] J. M. Lawrence, P. S. Riseborough, and R. D. Parks, Valence fluctuation phenomena, Rep. Prog. Phys. **44**, 1 (1981).

[3] T. E. Mason, G. Aeppli, A. P. Ramirez, K. N. Clausen, C. Broholm, N. Stücheli, E. Bucher, and T. T. M. Palstra, Spin Gap and Antiferromagnetic Correlations in the Kondo Insulator CeNiSn, Phys. Rev. Lett. **69**, 490 (1992).

[4] M. Dzero, K. Sun, V. Galitski, and P. Coleman, Topological Kondo Insulators, Phys. Rev. Lett. **104**, 106408 (2010).

[5] G. R. Stewart, Heavy-fermion systems, Rev. Mod. Phys. **56**, 755 (1984).

[6] N. D. Mathur, F. M. Grosche, S. R. Julian, I. R. Walker, D. M. Freye, R. K. W. Haselwimmer, and G. G. Lonzarich, Magnetically mediated superconductivity in heavy fermion compounds, Nature (London) **394**, 39 (1998).

[7] M. Somayazulu, M. Ahart, A. K. Mishra, Z. M. Geballe, M. Baldini, Y. Meng, V. V. Struzhkin, and R. J. Hemley, Evidence for Superconductivity above 260 K in Lanthanum Superhydride at Megabar Pressures, Phys. Rev. Lett. **122**, 027001 (2019).

[8] A. P. Drozdov, P. P. Kong, V. S. Minkov, S. P. Besedin, M. A. Kuzovnikov, S. Mozaffari, L. Balicas, F. F. Balakirev, D. E. Graf, V. B. Prakapenka, E. Greenberg, D. A. Knyazev, M. Tkacz, and M. I. Eremets, Superconductivity at 250 K in lanthanum hydride under high pressures, Nature (London) **569**, 528 (2019).

[9] R. W. Green, E. O. Thorland, J. Croat, and S. Legvold, Superconductivity in some compounds of La, Lu, Sc, and Y, J. Appl. Phys. **40**, 3161 (1969).

[10] A. L. Giorgi, E. G. Szklarz, M. C. Krupka, and N. H. Krikorian, Occurrence of superconductivity in lanthanum sesquicarbide, J. Less-Common Met. **17**, 121 (1969).

[11] T. L. Francavilla and F. L. Carter, Critical-magnetic-field curve of lanthanum sesquicarbide, Phys. Rev. B **14**, 128 (1976).

[12] J. S. Kim, R. K. Kremer, O. Jepsen, and A. Simon, Electronic and superconducting properties of the binary carbide La_2C_3, Curr. Appl. Phys. **6**, 897 (2006).

[13] M. Smidman, M. B. Salamon, H. Q. Yuan, and D. F. Agterberg, Superconductivity and spin-orbit coupling in non-centrosymmetric materials: A review, Rep. Prog. Phys. **80**, 036501 (2017).

[14] K. Kaminaga, D. Oka, T. Hasegawa, and T. Fukumura, Superconductivity of rock-salt structure LaO epitaxial thin film, J. Am. Chem. Soc. **140**, 6754 (2018).

[15] M. Mikami and S. Nakamura, Electronic structure of rare-earth sesquioxides and oxysulfides, J. Alloys Compd. **408-412**, 687 (2006).

[16] C. D. Wilk, High-κ gate dielectrics: Current status and materials properties considerations, J. Appl. Phys. **89**, 5243 (2001).

[17] G. Adachi and N. Imanaka, The binary rare earth oxides, Chem. Rev. **98**, 1479 (1998).

[18] P.-H. Sun, J.-F. Zhang, K. Liu, Q. Han, and Z.-Y. Lu, First-principles study of the superconductivity in LaO, Phys. Rev. B **104**, 045121 (2021).

[19] W. Li, J.-X. Zhu, Y. Chen, and C. S. Ting, First-principles calculations of the electronic structure of iron-pnictide $EuFe_2(As,P)_2$ superconductors: Evidence for antiferromagnetic spin order, Phys. Rev. B **86**, 155119 (2012).

[20] W. Li, X.-Y. Wei, J.-X. Zhu, C. S. Ting, and Y. Chen, Pressure induced topological quantum phase transition in Sb_2Se_3, Phys. Rev. B **89**, 035101 (2014).

[21] M. Zou, J. Chu, H. Zhang, T. Yuan, P. Cheng, W. Jin, D. Jiang, X. Xu, W. Yu, Z. An, X. Wei, G. Mu, and W. Li, Evidence the ferromagnetic order on CoSb layer of $LaCoSb_2$, Phys. Rev. B **101**, 155138 (2020).

[22] J. P. Perdew, K. Burke, and M. Ernzerhof, Generalized Gradient Approximation Made Simple, Phys. Rev. Lett. **77**, 3865 (1996).

[23] G. Kresse and J. Furthmüller, Efficient iterative schemes for *ab initio* total-energy calculations using a plane-wave basis set, Phys. Rev. B **54**, 11169 (1996).

[24] T. Yuan, M. Zou, W. Jin, X. Wei, X. Xu, and W. Li, Pairing symmetry in monolayer of othorhombic CoSb, Front. Phys. **16**, 43500 (2021).

[25] A. Togo and I. Tanaka, First principles phonon calculations in materials science, Scr. Mater. **108**, 1 (2015).

[26] W.-C. Huang, W. Li, and X. Liu, Exotic ferromagnetism in the two-dimensional quantum material C_3N, Front. Phys. **13**, 137104 (2018).

[27] J. M. Leger, N. Yacoubi, and J. Loriers, Synthesis of rare earth monoxides, J. Solid State Chem. **36**, 261 (1981).

[28] See Supplemental Material at http://link.aps.org/supplemental/10.1103/PhysRevB.105.L020508, which includes Refs. [29,30], for Figs. S1– S8 and Tables S1 and S2.

[29] D. M. Ceperley and B. J. Alder, Ground State of the Electron Gas by a Stochastic Method, Phys. Rev. Lett. **45**, 566 (1980).

[30] J. P. Perdew, J. A. Chevary, S. H. Vosko, K. A. Jackson, M. R. Pederson, D. J. Singh, and C. Fiolhais, Atoms, molecules, solids, and surfaces: Applications of the generalized gradient approximation for exchange and correlation, Phys. Rev. B **46**, 6671 (1992).

[31] S. M. Young, S. Zaheer, J. C. Y. Teo, C. L. Kane, E. J. Mele, and A. M. Rappe, Dirac Semimetal in Three Dimensions, Phys. Rev. Lett. **108**, 140405 (2012).

[32] T. O. Wehling, A. M. Black-Schaffer, and A. V. Balatsky, Dirac materials, Adv. Phys. **63**, 1 (2014).

[33] L. Fu, Topological Crystalline Insulators, Phys. Rev. Lett. **106**, 106802 (2011).

[34] H. Song, S.-J. Huang, L. Fu, and M. Hermele, Topological Phases Protected by Point Group Symmetry, Phys. Rev. X **7**, 011020 (2017).

[35] C. L. Kane and E. J. Mele, Z_2 Topological Order and the Quantum Spin Hall Effect, Phys. Rev. Lett. **95**, 146802 (2005).

[36] L. Fu, C. L. Kane, and E. J. Mele, Topological Insulators in Three Dimensions, Phys. Rev. Lett. **98**, 106803 (2007).

[37] J. E. Moore and L. Balents, Topological invariants of time-reversal-invariant band structures, Phys. Rev. B **75**, 121306(R) (2007).

[38] R. Roy, Topological phases and the quantum spin Hall effect in three dimensions, Phys. Rev. B **79**, 195322 (2009).

[39] L. Fu and C. L. Kane, Topological insulators with inversion symmetry, Phys. Rev. B **76**, 045302 (2007).

[40] B. R. Ortiz, S. M. L. Teicher, Y. Hu, J. L. Zuo, P. M. Sarte, E. C. Schueller, A. M. M. Abeykoon, M. J. Krogstad, S. Rosenkranz, R. Osborn, R. Seshadri, L. Balents, J. He, and S. D. Wilson, CsV_3Sb_5: A $\mathbb{Z}_2$ Topological Kagome Metal with a Superconducting Ground State, Phys. Rev. Lett. **125**, 247002 (2020).

[41] B. R. Ortiz, P. M. Sarte, E. M. Kenney, M. J. Graf, S. M. L. Teicher, R. Seshadri, and S. D. Wilson, Superconductivity in the $\mathbb{Z}_2$ kagome metal KV_3Sb_5, Phys. Rev. Materials **5**, 034801 (2021).

[42] D. Kasinathan, K. Koepernik, L. H. Tjeng, and M. W. Haverkort, SmO thin films: A flexible route to correlated flat bands with nontrivial topology, Phys. Rev. B **91**, 195127 (2015).

[43] M. S. Dresselhaus, G. Dresselhaus, and A. Jorio, *Group Theory: Application to the Physics of Condensed Matter* (Springer-Verlag, Berlin, 2008).

[44] F. Lu, J. Zhao, H. Weng, Z. Fang, and X. Dai, Correlated Topological Insulators with Mixed Valence, Phys. Rev. Lett. **110**, 096401 (2013).

[45] M. Dzero, J. Xia, V. Galitski, and P. Coleman, Topological Kondo insulators, Annu. Rev. Condens. Matter Phys. **7**, 249 (2016).

[46] M. Fleck, A. M. Oleś, and L. Hedin, Magnetic phases near the Van Hove singularity in *s*- and *d*-band Hubbard models, Phys. Rev. B **56**, 3159 (1997).

[47] B. I. Halperin, Quantized Hall conductance, current-carrying edge states, and the existence of extended states in a two-

dimensional disordered potential, Phys. Rev. B **25**, 2185 (1982).

[48] Y. Hatsugai, Chern Number and Edge States in the Integer Quantum Hall Effect, Phys. Rev. Lett. **71**, 3697 (1993).

[49] M. P. Lopez Sancho, J. M. Lopez Sancho, J. M. L. Sancho, and J. Rubio, Highly convergent schemes for the calculation of bulk and surface Green functions, J. Phys. F **15**, 851 (1985).

[50] W. Li, J. Zang, and Y. Jiang, Size effects on transport properties in topological Anderson insulators, Phys. Rev. B **84**, 033409 (2011).

[51] N. Marzari and D. Vanderbilt, Maximally localized generalized Wannier functions for composite energy bands, Phys. Rev. B **56**, 12847 (1997).

[52] I. Souza, N. Marzari, and D. Vanderbilt, Maximally localized Wannier functions for entangled energy bands, Phys. Rev. B **65**, 035109 (2001).

[53] Q. Wu, S. Zhang, H.-F. Song, M. Troyer, and A. A. Soluyanov, WannierTools: An open-source software package for novel topological materials, Comput. Phys. Commun. **224**, 405 (2018).

[54] L. Fu and C. L. Kane, Superconducting Proximity Effect and Majorana Fermions at the Surface of a Topological Insulator, Phys. Rev. Lett. **100**, 096407 (2008).

[55] C. Nayak, S. H. Simon, A. Stern, M. Freedman, and S. Das Sarma, Non-Abelian anyons and topological quantum computation, Rev. Mod. Phys. **80**, 1083 (2008).

[56] J. Alicea, New directions in the pursuit of Majorana fermions in solid state systems, Rep. Prog. Phys. **75**, 076501 (2012).

[57] C. W. J. Beenakker, Search for Majorana fermions in superconductors, Annu. Rev. Condens. Matter Phys. **4**, 113 (2013).

[58] G. Xu, B. Lian, P. Tang, X.-L. Qi, and S.-C. Zhang, Topological Superconductivity on the Surface of Fe-Based Superconductors, Phys. Rev. Lett. **117**, 047001 (2016).

[59] S. Zhu, L. Kong, L. Cao, H. Chen, S. Du, Y. Xing, W. Liu, D. Wang, C. Shen, F. Yang, J. Schneeloch, R. Zhong, G. Gu, L. Fu, Y.-Y. Zhang, H. Ding, and H.-J. Gao, Nearly quantized conductance plateau of vortex zero mode in an iron-based superconductor, Science **367**, 189 (2019).

[60] T. Meng and L. Balents, Weyl superconductors, Phys. Rev. B **86**, 054504 (2012).